Probing mid-infrared surface interface states based on thermal emission

FAN ZHONG,[1,2,3,4] **YE ZHANG,**[2,3] **SHINING ZHU,**[2] **AND HUI LIU**[2,5]

[1] *School of Physics, Southeast University, Nanjing 211189, China*
[2] *National Laboratory of Solid State Microstructures & School of Physics, Collaborative Innovation Center of Advanced Microstructures, Nanjing University, Nanjing, Jiangsu 210093, China*
[3] *These authors contributed equally to this work*
[4] *zhongfan@seu.edu.cn*
[5] *liuhui@nju.edu.cn*

Abstract: Probing mid-infrared surface wave radiation remains a big challenge for a long time. The lack of convenient and quick mid-infrared surface wave radiation probing methods limits the development of the integrated mid-infrared materials and devices. In this work, we propose a scheme to construct and probe the mid-infrared surface wave radiation of interface state in the waveguide through thermal emission. A superlattice composed of alternately placed periodic meta-crystals is designed to construct an array of interfaces to realize the interface states through the transverse electrical waveguide modes with a tolerance in structural parameters. By heating the structure, we employ angular resolved thermal emission spectroscopy to directly and quickly verify the dispersion of mid-infrared interface states, which have specific frequencies, angles, and polarizations. Moreover, we establish a thermal imaging microscopy to probe the local waveguide interface state directly for the first time. This proposed infrared probing method based on thermal emission can be generalized to probe the mid-infrared surface wave in other systems, such as surface plasmon waves in graphene or surface phonon waves in two-dimensional materials in the mid-infrared range.

1. Introduction

The radiation effect of surface wave has important applications in the fields of molecular imaging, molecular sensing, and heat transfer [1]. Therefore, the detection and control of surface wave radiation is of great significance in practical applications. At present, plenty of developed technologies are used to probe the surface wave in the visible, near-infrared and microwave range. For example, near-field scanning optical microscopy, fluorescence imaging, and cathodoluminescence imaging spectroscopy are used to probe the surface wave in the visible and near-infrared range [2–5], and microwave antennas are used to probe the surface wave in the microwave range [6,7]. However, there has always been a dearth of simple or flexible experimental techniques to probe the surface wave radiation in the mid-infrared range without infrared source.

In order to probe infrared surface wave, people invented the scattering-type scanning near-field optical microscopy to experimentally access high-quality surface wave by illuminating the sharp tip of an atomic force microscope with a focused infrared beam [8–11]. It is used to probe surface plasmon wave in graphene and surface phonon wave in two-dimensional materials in the mid-infrared range. Such a technique requires an external infrared laser source, and the corresponding validity depends on the collimation and coherence of the light source. The working infrared frequency range is quite limited because the infrared laser source is quite scarce. Therefore, it is critical to pursue a simple and widely applicable technique, free of an external light source, to probe mid-infrared surface waves.

Meanwhile, since the blackbody radiation is universal for the materials above the absolute zero, the control of the thermal emissions is important. Many promising applications in manipulating thermal emissions in artificial materials provide solutions for the problems in thermal sensing and imaging [12], thermal camouflaging [13,14], incandescent sources [15], narrow-band infrared light sources [16–20], radiation cooling [21–26], thermophotovoltaic devices [27,28], super-Planckian near-field thermal radiation [29], solar desalination [30,31], and so on. These thermal manipulations are mainly based on the corresponding optical systems, such as photonic crystals [32], metamaterials [33–36], and surface plasmons [37].

In this research, a method based on the thermal emission was proposed to probe the mid-infrared surface wave radiation of the interface state in a planar meta-crystal. We used the angular resolved thermal emission spectroscopy (ARTES) to detect the band dispersion of the mid-infrared interface state. Furthermore, we established a thermal imaging microscopy system to directly probe the local waveguide interface state (WIS) mainly located at the place around the germanium/air surface between two meta-crystals for the first time. This technique can probe the infrared surface wave radiation without the need of external infrared source excitation. The probing frequency range is broadband, which can cover near-infrared and mid-infrared wavelength. Compared with other infrared surface wave probing techniques, this technique is simple and extensible. In addition to waveguide modes, this technique can be easily extended to detect other infrared surface wave radiation, such as graphene surface plasmon and surface phonons in boron nitride.

2.   Design, simulation, and experiment

2.1.   Structure design

In this work, we designed a superlattice composed of periodic meta-crystals to produce WISs. This superlattice is shown in Fig. 1(a), and the corresponding fabrication process is shown in the Supplement 1 [38]. Figure 1(b) shows the details of the interface between two meta-crystals. For a meta-crystal with a multilayer structure, by adjusting the corresponding geometric parameters of the gold cladding grating and the Ge layer, the dispersion of the transverse electrical (TE) guided mode inside the Ge layer could be controlled due to the change of the effective mode index of the multilayer structure [39], and only TE mode was considered in this work. The gold blocks inside the Ge layer significantly enhanced the contrast of the refractive index between two guided modes in the Ge layer to construct meta-crystals and to open the band gap.

To construct an interface state, two kinds of one-dimensional periodic meta-crystals with a mirror symmetric unit cell (like three layers, "ABA") [40] and with a common band gap were needed. However, the symmetric properties of their band edge modes were different (and could also be interpreted by the Zak phase in topological language [40–42]). One of the meta-crystals needed to have a band gap for which the upper edge had odd symmetry and the lower edge had even symmetry, while the symmetries in the other meta-crystal were swapped [41,42]. To achieve this dispersion, in addition to each layer's thickness, the periods and widths of the gold grating were also tunable parameters in the design. Based on these conditions, there was a tolerance in structural parameters. Therefore, in our scheme, the two different meta-crystals shown in Fig. 1(a, b) were designed with different periods and duty cycles, and they shared the same thickness of the Ge and Au layers for convenience in fabrication. Figure 1(c) shows a cross-section view of a small portion of the whole sample. The schematic picture of experiment is shown in Fig. 1(d).

2.2.   Control of the thermal emission through the WIS

The detected thermal emission originated from the radiative loss (low confinement), while this loss could be ignored in designing the planar structure, and the non-Hermitian situation was not considered. Moreover, by changing the structural parameters, both the angle and the frequency of
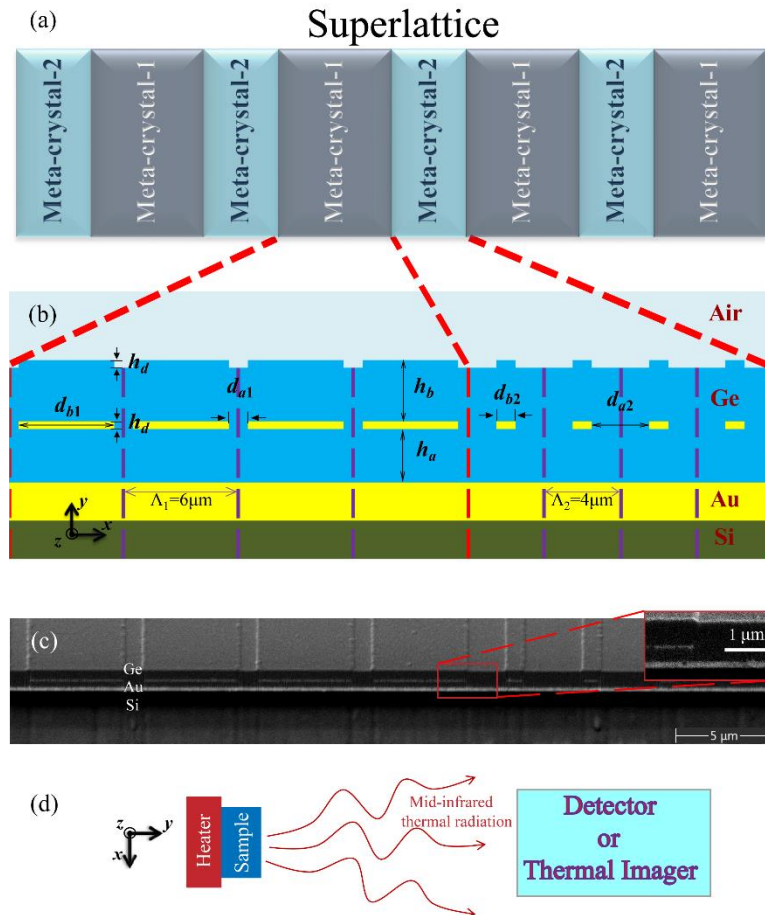
Fig. 1. Waveguide interfaces in superlattice. (a) Schematic picture of superlattice. (b) Cross-section picture of the planar structure on a 200-nm gold layer deposited on a silicon wafer with structural parameters $h_a = 0.45$ μm, $h_b = 0.65$ μm, $h_d = 70$ nm, and period $\Lambda = 4\Lambda_1 + 4\Lambda_2 = 40$ μm, where $\Lambda_1 = (d_{a1} + d_{b1}) = 6$ μm, $d_{b1} = 5$ μm, $\Lambda_2 = (d_{a2} + d_{b2}) = 4$ μm, and $d_{b2} = 1$ μm. The large period has four unit cells for the first design and four unit cells for the second design. The red dashed lines denote two interfaces in a period, and the purple dashed lines separate the large cell into small units. (c) SEM picture of the cross section of the structure. (d) Schematic picture of experiment.
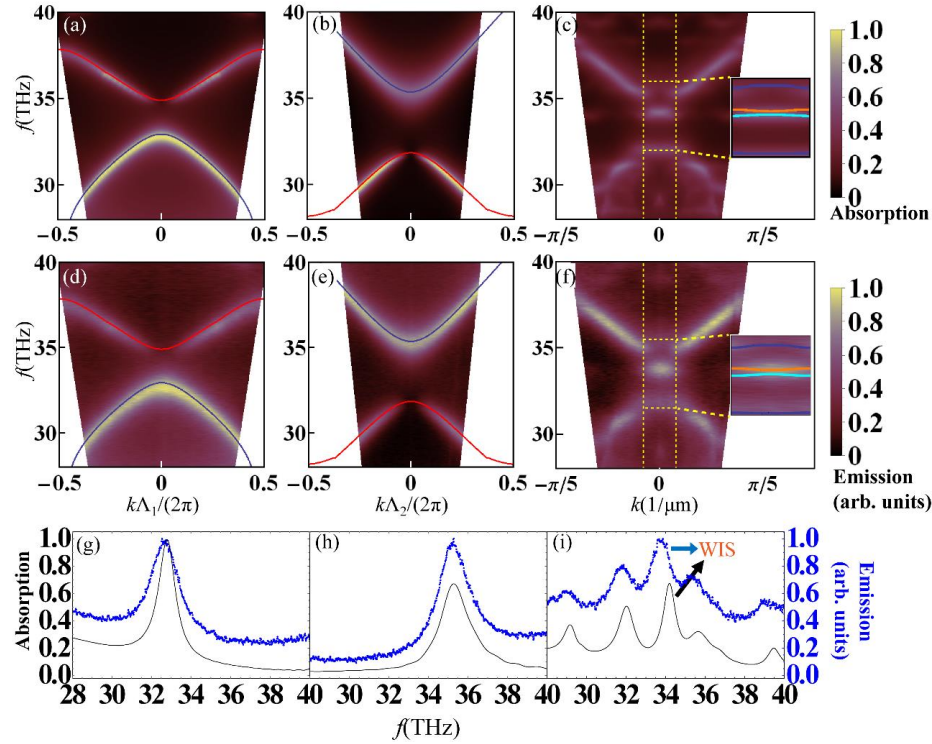
Fig. 2. Simulations and experiments for WISs. (a–c) Optical absorption (density map) simulated by FDTD simulations with realistic material parameters ("Au-Palik" and "Ge-Palik" from the FDTD material database [43]). (d–f) Measured thermal emission with sample at 100°C (density map). The red, blue, cyan, and orange lines in (a-f) are eigenfrequencies calculated by COMSOL with the Drude model [$\varepsilon_{Au} = 1 - \omega_p^2/(\omega^2 + i\omega\omega_c)$, $\omega_p = 9.0$ eV, and $\omega_c = 0.027$ eV] and $\varepsilon_{Ge} = 16.04$. Here, $h_a = 0.45$ μm, $h_d = 70$ nm, $h_b = 0.65$ μm (except for $h_b = 0.67$ μm in (f)). (a, d) Periodic structure with the period Λ_1 of 6 μm and the metal width of 5 μm (meta-crystal-1). (b, e) Periodic structure with the period Λ_2 of 4 μm and the metal width of 1 μm (meta-crystal-2). (c, f) WISs (cyan and orange lines) in the superlattice composed of meta-crystals in (a) and (b), as shown in Fig. 1. The vertical yellow dashed lines in these figures mark the first Brillouin zone, and k is in x-direction. (g), (h), and (i) show the extracted simulated absorption (plotted in black line) and experimental emission (blue points) spectra from (a, d), (b, e), and (c, f), respectively, when $k=0$. WIS appears around 34THz in (i). Although there exists the background noise in experiments, the results still have a good match with simulations

the thermal emission could be manipulated through the TE mode (E_z, selected by a polarizer) in the designed meta-crystals. The experimental and corresponding simulated results are compared in Fig. 2. Figure 2(a) shows the finite-difference time-domain (FDTD) simulation results of the optical absorption of the meta-crystal with periodic structures (only one kind of unit cell with $\Lambda_1 = 6$ μm, $d_{b1} = 5$ μm) using the commercial software Lumerical FDTD [43]. The results were given as a density map. It was not easy to calculate the far-field thermal radiation directly. Due to Kirchhoff's law, the optical absorption was the reverse process of the thermal emission, which could be calculated as E = A = 1-R-T (E is emissivity; A is absorptivity; R is reflectivity; T is transmissivity, and T is 0 here). We noticed that when $k = 0$, the upper band edge had minimum emission due to the odd symmetry of the corresponding eigenmode, which was mismatched

with the free space, and the lower band edge had a bright mode due to the even symmetry of the corresponding eigenmode [39]. The plotted red and blue lines in Fig. 2(a) represent the bands calculated with the commercial software COMSOL [44], and the different colors denote the different symmetries at $k = 0$, as shown in Fig. S1(a) in the Supplement 1 [38]. A comparison between the eigenfrequencies calculated by COMSOL and the ARTES (details are shown in the Supplement 1 [38]) measurements is shown in Fig. 2(d). This comparison indicates the consistency of the simulations and the measurements. The operations were repeated for the other meta-crystal with its unit cell's parameters $\Lambda_2 = 4$ μm and $d_{b2} = 1$ μm, and results are shown in Figs. 2(b), 2(e). In this meta-crystal, the symmetries of the band edge swapped their positions compared with those in the first meta-crystal, as shown in Fig. S1(b) in the Supplement 1 [38].

The leakage of the WISs, which was narrow in terms of the frequency and angle, could be detected through the thermal emission from interfaces that were constructed with the two kinds of meta-crystals presented in the above discussion and shown in Fig. 1. Figure 2(c) shows the FDTD simulations of the absorption, and the insert picture shows the data inside the yellow dashed lines with the dispersion calculated by COMSOL. The orange and cyan lines denote the WISs. Because of the coupling between the two interfaces in one period, the dispersion of the WISs split into two branches. When $k = 0$, the eigenmode calculated by COMSOL on the orange line had even symmetry (as shown in Fig. S2(b) in the Supplement 1 [38]) and it radiated to the far field, while the eigenmode on the cyan line had the opposite symmetry and it could not radiate to the far field (as shown in Fig. S2(a) in the Supplement 1 [38]), while in the FDTD simulation, two modes could not be distinguished because of the similarity in the frequency. The two blue lines at the edge of the figure show the boundaries of the bulky band. In the experiment, the ARTES was used to record the thermal emission signals of the WIS whose frequency was nearly independent of k in x-direction ($k = k_0 \sin\theta$, where k_0 is wave vector in vacuum, and θ is rotational angle around the z-axis in Fig. 1(b)) and whose main energy was limited within $\pm 7°$, as shown in Fig. 2(f). Owing to the fabrication in the experiments, h_b was about 0.67 μm in this case, similar to the results shown in Fig. 2(c), and the WIS still appeared in the shared gap, as predicted by COMSOL. The WIS in the thermal radiation had the properties of a narrow frequency range and emission angle. The direct comparisons between experiments and simulations are shown in Figs. 2(g)–2(i), where the background noise in experiments could be ignored and the interface states had more efficient radiation than the nearby bulky region. The displacement of WIS in frequency between the simulated and experimental results is mainly from the deviation in fabrication process.

2.3. *Thermal imaging of the WIS*

The WIS that we constructed in the metasurface could be directly visualized in the thermal imaging microscopy system, which was also regarded as a direct proof of the WIS. The structures in this sample consisted of two kinds of unit cells, which are also shown in Fig. 1(b), while in this time there was only one interface, as shown in Fig. 3(a). The eigenfrequencies and the eigenmode field patterns of the structure in Fig. 3(a) were calculated by COMSOL, and only one WIS was found as shown in Fig. S2(c) [38], where the localized Ez profile around the interface means the localization of energy in x-direction for this interface state. The corresponding scanning electron microscopy (SEM) picture of the sample with the same fabrication process is shown in Fig. 3(b) with the top view. A thermal imaging camera, Fotric 288, was applied in our thermal imaging microscopy system to visualize the temperature distribution of the front view. The sample embedded in the heater was heated to 200 ℃ with an environmental temperature at 0 ℃ to decrease the background noise, and the thermal emission travelled through a polarizer in order to select the TE mode and a filter with a center wavelength at 8.9 micros and a full width at half maximum of 500 nm (BP-8900-500 nm from Spectrogon) to select the frequencies around the WIS. The thermal imaging microscopy system provided the two-dimensional color map of

the temperature around the interface, as shown in Fig. 3(c). The temperature map provided the information of the thermal emission energy around 8.9 μm with a calibration of 0.1 ℃. The detailed data denoted by a pink dashed line are shown in Fig. 3(d). The point data in Fig. 3(d) were obtained from the experiments and the blue line was fitted by assuming that the temperature around the interface had a Gaussian distribution and that the two sides of the interface had each basic temperature with a gradient at the conjunction. The temperature of the interface was a local maximum, while by changing the center wavelength of the filter, the WIS disappeared in the temperature map. To confirm this scheme, the measurements of the reflection (normal incidence and emissivity=1-reflectivity) were conducted before thermal imaging in three areas of the sample. The left side and the right side of Fig. 3(e) present the corresponding reflections conducted in the areas on the left side and the right side of the interface, respectively. Additionally, another measurement conducted in the area containing the interface is shown in the middle area in Fig. 3(e). The detected reflections could be predicted by the simulations in Figs. 2(g)-2(i), and the corresponding simulations are denoted by black lines in Fig. 3(e). In the middle image of Fig. 3(e), the difference between the experimental reflectivity and the simulated reflectivity mainly results from the density of the interfaces (the selection box in this experiment is about 60 μm in x-direction to contain the interface, and the simulation of periodic structure contains two interfaces per 40 μm in x-direction). These experimental results directly offered a scheme to visualize the WIS through a thermal imaging system. Moreover, the thermal images could be designed by using the characteristics of the WIS and encrypted by using the frequency, the polarization, and the environmental temperature, which also paved the way for the encryption of infrared displays.

2.4. Variability of the WIS

If we changed the thickness of h_b of the sample shown in Fig. 1(c), we could tune the WIS in a range of more than 4 THz. In Fig. 4(a), the blue and red areas were obtained from the periodic samples by continuously increasing the thickness of the top Ge layer h_b (results of specific h_b shown in Figs. 2(a), 2(b)). We took the case $h_b = 0.65$ μm as an example, for which the red areas corresponding to bulky band were obtained from the band structure of the sample in Fig. 2(a), while the blue areas were from the band structure of the sample in Fig. 2(b). With the increasing of h_b, the two band gaps became smaller and the shared gap disappeared, and the WISs marked by orange and cyan lines shifted their frequency. As shown in Figs. 4(b)–4(d), the sample shown in Fig. 1(c) was tested for different values of h_b. With the increasing of h_b, the frequencies of the WISs decreased and the energy angular distribution of the WISs shrank as shown in Figs. 4(b), 4(c). If h_b was large enough, the interface states merged into the bulky band and lost their localization as shown in Fig. 4(d), leading to the disappearance of WISs in the thermal imaging.

The WIS was guaranteed at an interface with meta-crystals that had proper topological characteristics regardless of the specific structural parameters, and the flexibility of the parameters in the design shifted the frequency and angular distribution of WIS, as shown in Fig. S3 in the Supplement 1 [38]. However, in our scheme, the WISs were only confined in the x-direction, while they propagated along the z-direction, as shown in Fig. S4 in the Supplement 1 [38]. The parabolic dispersions of the WISs represented no localization in the z-direction, and the WISs shifted their frequencies when k_z changed.
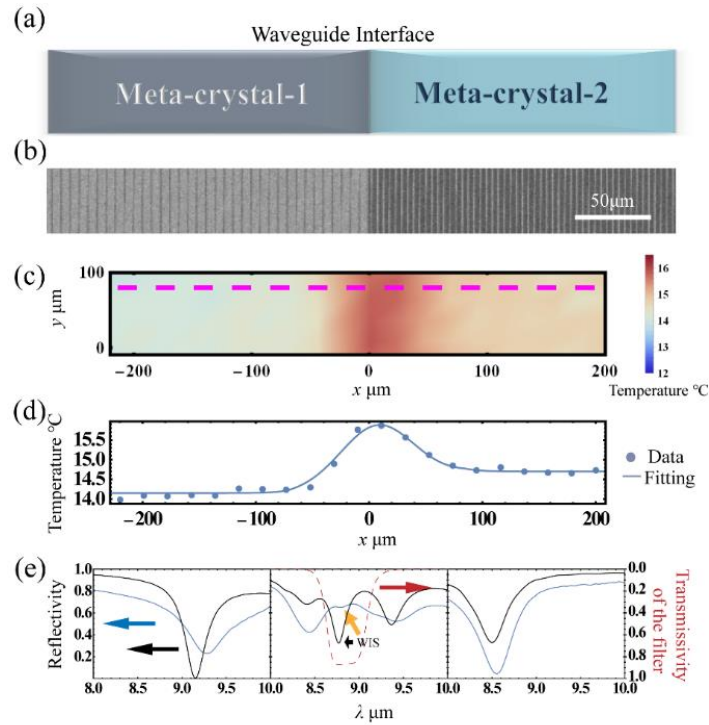
Fig. 3. Direct observation of a single TE WIS. (a) Schematic picture of a single waveguide interface. (b) The SEM picture of the top view of the interface before the top layer Ge is covered. (c) Thermal imaging of the sample at 200°C with an environmental temperature of 0°C with filters in wavelength and polarization. The image was acquired without correction in emissivity. The red region denotes the interface state. (d) shows the detailed data (the line is the fitting of the points from the experiments) of the pink dashed line in (c), where the temperature on the interface was about 1.7°C higher than that on the left part and about 1.2°C higher than that on the right part with a calibration of about 0.1 °C in measurement. (e) The blue lines are the measured TE reflection (normal incidence) of the sample with a single waveguide interface (emissivity=1-reflectivity); the black lines are the simulation predictions (normal incidence) through periodic structures used in Figs. 2(a)-2(c), which has differences compared to experimental result of a single interface in the middle image; and the red dashed line is the transmissivity of the filter with inversed *y*-axis in order to compare with the emissivity. The blue line in the left image shows the experimental result of the periodic structure, meta-crystal-1, that was on the left side of the interface. The blue line in the middle image shows the reflection of the area containing the interface. The blue line in the right image shows the experimental result of the periodic structure, meta-crystal-2, which was on the right side of the interface.
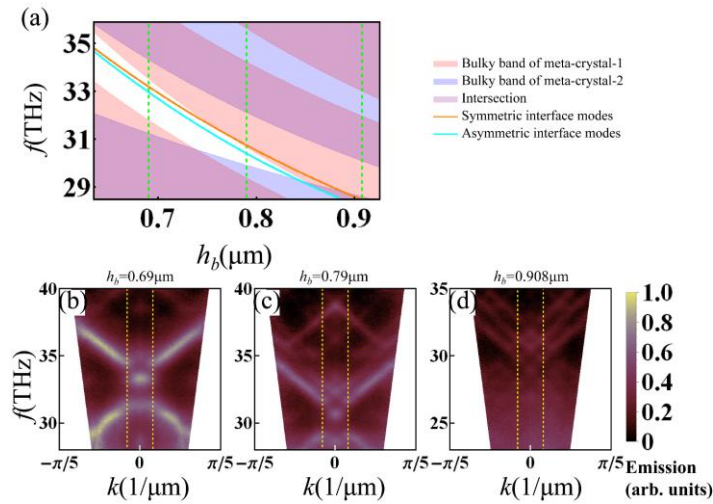
Fig. 4. Variability of the waveguide interface states. (a) Eigenfrequencies calculated by COMSOL for the superlattice with interface states (orange and cyan lines) and the corresponding meta-crystals (red and blue areas), where the top Ge layer varied from 0.64 μm to 0.92 μm at $k = 0$. The other structural parameters (except for h_b) are the same as shown in Fig. 1. (b–d) Experimental results of the thermal emission of the meta-crystal, when (b) $h_b = 0.69$ μm, (c) $h_b = 0.79$ μm, (d) $h_b = 0.908$ μm. The interface states disappeared with the increase of the top Ge layer. The vertical yellow dashed lines in these figures mark the first Brillouin zone, and k is in x-direction.

3. Conclusion

In this work, we designed and experimentally produced mid-infrared polarized surface waves based on a superlattice with periodic interfaces, and we measured its radiation through the ARTES. Moreover, we established a thermal imaging microscopy system to visualize the WIS with temperature distribution. Importantly, there was no external infrared source needed in this probing method, which simplifies the measurement.

Based on the point view that thermal emission is the time-reversal process of optical absorption, WISs in a superlattice can be revealed through ARTES. The interface state had isolated emission signals in the band mapping. The thermal emission frequency and angular distribution of WIS could be tuned by changing the thickness of the cover layer on the superlattice. As shown in the band mapping and the thermal imaging, the interface state could be turned off when the covered layer was thick enough. The proposed probing scheme shows that the localized interface state can be probed by detecting the changes in the angles, intensities, and frequencies of the thermal signals in the far field, which might provide a new method for thermal sensing. In addition, this designable far-field emission based on structural properties also provides an editable temperature pattern which can be controlled by the environmental temperature, polarization, and the detected range in the wavelength, and these may lead to a prospective future for thermal displays.

Disclosures. The authors declare no conflicts of interest

Data availability. Data underlying the results presented in this paper are not publicly available at this time but may be obtained from the authors upon reasonable request.

Supplemental document. See Supplement 1 for supporting content.

References

1. Y.-W. Huang, H.-X. Xu, S. Sun, Y. Wu, Z. Wang, S. Xiao, W. X. Jiang, T. J. Cui, D. P. Tsai, and C.-W. Qiu, "Structured Semiconductor Interfaces: Active Functionality on Light Manipulation," Proc. IEEE **108**(5), 772–794 (2020).
2. M. Kuttge, W. Cai, F. J. García de Abajo, and A. Polman, "Dispersion of metal-insulator-metal plasmon polaritons probed by cathodoluminescence imaging spectroscopy," Phys. Rev. B **80**(3), 033409 (2009).
3. P. Genevet, D. Wintz, A. Ambrosio, A. She, R. Blanchard, and F. Capasso, "Controlled steering of Cherenkov surface plasmon wakes with a one-dimensional metamaterial," Nat. Nanotechnol. **10**(9), 804–809 (2015).
4. S. Xiao, F. Zhong, H. Liu, S. Zhu, and J. Li, "Flexible coherent control of plasmonic spin-Hall effect," Nat. Commun. **6**(1), 8360 (2015).
5. C. Sheng, H. Liu, H. Chen, and S. Zhu, "Definite photon deflections of topological defects in metasurfaces and symmetry-breaking phase transitions with material loss," Nat. Commun. **9**(1), 4271 (2018).
6. Z. Wang, Y. Chong, J. D. Joannopoulos, and M. Soljacic, "Observation of unidirectional backscattering-immune topological electromagnetic states," Nature **461**(7265), 772–775 (2009).
7. A. B. Khanikaev and G. Shvets, "Two-dimensional topological photonics," Nat. Photonics **11**(12), 763–773 (2017).
8. R. Hillenbrand, T. Taubner, and F. Keilmann, "Phonon-enhanced light matter interaction at the nanometre scale," Nature **418**(6894), 159–162 (2002).
9. Z. Fei, A. S. Rodin, G. O. Andreev, W. Bao, A. S. McLeod, M. Wagner, L. M. Zhang, Z. Zhao, M. Thiemens, G. Dominguez, M. M. Fogler, A. H. Castro Neto, C. N. Lau, F. Keilmann, and D. N. Basov, "Gate-tuning of graphene plasmons revealed by infrared nano-imaging," Nature **487**(7405), 82–85 (2012).
10. F. Lu, M. Jin, and M. A. Belkin, "Tip-enhanced infrared nanospectroscopy via molecular expansion force detection," Nat. Photonics **8**(4), 307–312 (2014).
11. H. A. Bechtel, E. A. Muller, R. L. Olmon, M. C. Martin, and M. B. Raschke, "Ultrabroadband infrared nanospectroscopic imaging," Proc. Natl. Acad. Sci. U S A **111**(20), 7191–7196 (2014).
12. X. Tang, M. M. Ackerman, M. Chen, and P. Guyot-Sionnest, "Dual-band infrared imaging using stacked colloidal quantum dot photodiodes," Nat. Photonics **13**(4), 277–282 (2019).
13. R. Hu, W. Xi, Y. Liu, K. Tang, J. Song, X. Luo, J. Wu, and C.-W. Qiu, "Thermal camouflaging metamaterials," Mater. Today **45**, 120–141 (2021).
14. H. Zhu, Q. Li, C. Tao, Y. Hong, Z. Xu, W. Shen, S. Kaur, P. Ghosh, and M. Qiu, "Multispectral camouflage for infrared, visible, lasers and microwave with radiative cooling," Nat. Commun. **12**(1), 1805 (2021).
15. O. Ilic, P. Bermel, G. Chen, J. D. Joannopoulos, I. Celanovic, and M. Soljacic, "Tailoring high-temperature radiation and the resurrection of the incandescent source," Nat. Nanotechnol. **11**(4), 320–324 (2016).
16. X. Liu, T. Starr, A. F. Starr, and W. J. Padilla, "Infrared spatial and frequency selective metamaterial with near-unity absorbance," Phys. Rev. Lett. **104**(20), 207403 (2010).
17. X. Liu, T. Tyler, T. Starr, A. F. Starr, N. M. Jokerst, and W. J. Padilla, "Taming the blackbody with infrared metamaterials as selective thermal emitters," Phys. Rev. Lett. **107**(4), 045901 (2011).
18. A. Hugi, G. Villares, S. Blaser, H. C. Liu, and J. Faist, "Mid-infrared frequency comb based on a quantum cascade laser," Nature **492**(7428), 229–233 (2012).
19. C. Wu, N. Arju, G. Kelp, J. A. Fan, J. Dominguez, E. Gonzales, E. Tutuc, I. Brener, and G. Shvets, "Spectrally selective chiral silicon metasurfaces based on infrared Fano resonances," Nat. Commun. **5**(1), 3892 (2014).
20. D. Ding and A. J. Minnich, "Selective radiative heating of nanostructures using hyperbolic metamaterials," Opt. Express **23**(7), A299–308 (2015).
21. A. P. Raman, M. A. Anoma, L. Zhu, E. Rephaeli, and S. Fan, "Passive radiative cooling below ambient air temperature under direct sunlight," Nature **515**(7528), 540–544 (2014).
22. N. N. Shi, C. C. Tsai, F. Camino, G. D. Bernard, N. Yu, and R. Wehner, "Thermal physiology. Keeping cool: Enhanced optical reflection and radiative heat dissipation in Saharan silver ants," Science **349**(6245), 298–301 (2015).
23. Y. Zhai, Y. Ma, S. N. David, D. Zhao, R. Lou, G. Tan, R. Yang, and X. Yin, "Scalable-manufactured randomized glass-polymer hybrid metamaterial for daytime radiative cooling," Science **355**(6329), 1062–1066 (2017).
24. X. Yin, R. Yang, G. Tan, and S. Fan, "Terrestrial radiative cooling: Using the cold universe as a renewable and sustainable energy source," Science **370**(6518), 786–791 (2020).
25. D. Li, X. Liu, W. Li, Z. Lin, B. Zhu, Z. Li, J. Li, B. Li, S. Fan, J. Xie, and J. Zhu, "Scalable and hierarchically designed polymer film as a selective thermal emitter for high-performance all-day radiative cooling," Nat. Nanotechnol. **16**(2), 153–158 (2021).
26. S. Zeng, S. Pian, M. Su, Z. Wang, M. Wu, X. Liu, M. Chen, Y. Xiang, J. Wu, M. Zhang, Q. Cen, Y. Tang, X. Zhou, Z. Huang, R. Wang, A. Tunuhe, X. Sun, Z. Xia, M. Tian, M. Chen, X. Ma, L. Yang, J. Zhou, H. Zhou, Q. Yang, X. Li, Y. Ma, and G. Tao, "Hierarchical-morphology metafabric for scalable passive daytime radiative cooling," Science **373**(6555), 692–696 (2021).

27. A. Lenert, D. M. Bierman, Y. Nam, W. R. Chan, I. Celanovic, M. Soljacic, and E. N. Wang, "A nanophotonic solar thermophotovoltaic device," Nat. Nanotechnol. **9**(2), 126–130 (2014).

28. A. Fiorino, L. Zhu, D. Thompson, R. Mittapally, P. Reddy, and E. Meyhofer, "Nanogap near-field thermophotovoltaics," Nat. Nanotechnol. **13**(9), 806–811 (2018).

29. J. Yang, W. Du, Y. Su, Y. Fu, S. Gong, S. He, and Y. Ma, "Observing of the super-Planckian near-field thermal radiation between graphene sheets," Nat. Commun. **9**(1), 4033 (2018).

30. L. Zhou, Y. Tan, J. Wang, W. Xu, Y. Yuan, W. Cai, S. Zhu, and J. Zhu, "3D self-assembly of aluminium nanoparticles for plasmon-enhanced solar desalination," Nat. Photonics **10**(6), 393–398 (2016).

31. A. Politano, P. Argurio, G. Di Profio, V. Sanna, A. Cupolillo, S. Chakraborty, H. A. Arafat, and E. Curcio, "Photothermal Membrane Distillation for Seawater Desalination," Adv. Mater. **29**(2), 1603504 (2017).

32. M. De Zoysa, T. Asano, K. Mochizuki, A. Oskooi, T. Inoue, and S. Noda, "Conversion of broadband to narrowband thermal emission through energy recycling," Nat. Photonics **6**(8), 535–539 (2012).

33. Y. Guo, C. L. Cortes, S. Molesky, and Z. Jacob, "Broadband super-Planckian thermal emission from hyperbolic metamaterials," Appl. Phys. Lett. **101**(13), 131106 (2012).

34. D. Costantini, A. Lefebvre, A. L. Coutrot, I. Moldovan-Doyen, J. P. Hugonin, S. Boutami, F. Marquier, H. Benisty, and J. J. Greffet, "Plasmonic Metasurface for Directional and Frequency-Selective Thermal Emission," Phys. Rev. Appl. **4**(1), 014023 (2015).

35. K. K. Du, Q. Li, Y. B. Lyu, J. C. Ding, Y. Lu, Z. Y. Cheng, and M. Qiu, "Control over emissivity of zero-static-power thermal emitters based on phase-changing material GST," Light: Sci. Appl. **6**(1), e16194 (2017).

36. J. Park, J. H. Kang, X. Liu, S. J. Maddox, K. Tang, P. C. McIntyre, S. R. Bank, and M. L. Brongersma, "Dynamic thermal emission control with InAs-based plasmonic metasurfaces," Sci. Adv. **4**(12), eaat3163 (2018).

37. F. B. Barho, F. Gonzalez-Posada, M. Bomers, A. Mezy, L. Cerutti, and T. Taliercio, "Surface-Enhanced Thermal Emission Spectroscopy with Perfect Absorber Metasurfaces," ACS Photonics **6**(6), 1506–1514 (2019).

38. See the Supplemental Material for details

39. F. Zhong, K. Ding, Y. Zhang, S. Zhu, C. T. Chan, and H. Liu, "Angle-Resolved Thermal Emission Spectroscopy Characterization of Non-Hermitian Metacrystals," Phys. Rev. Appl. **13**(1), 014071 (2020).

40. Q. Wang, M. Xiao, H. Liu, S. Zhu, and C. T. Chan, "Measurement of the Zak phase of photonic bands through the interface states of a metasurface/photonic crystal," Phys. Rev. B **93**(4), 041415 (2016).

41. M. Xiao, Z. Q. Zhang, and C. T. Chan, "Surface Impedance and Bulk Band Geometric Phases in One-Dimensional Systems," Phys. Rev. X **4**, 021017 (2014).

42. M. Xiao, G. Ma, Z. Yang, P. Sheng, Z. Q. Zhang, and C. T. Chan, "Geometric phase and band inversion in periodic acoustic systems," Nat. Phys. **11**(3), 240–244 (2015).

43. Lumerical Solutions, Inc. http://www.lumerical.com/tcadproducts/fdtd/.

44. Computer code COMSOL MULTI-PHYSICS 5.3 (developed by COMSOL Inc., Burlington, VT, 2017).